

ARTICLE

<https://doi.org/10.1038/s41467-019-09021-3>

OPEN

# Unraveling the mysterious failure of Cu/SAPO-34 selective catalytic reduction catalysts

Aiyong Wang<sup>1</sup>, Ying Chen<sup>2</sup>, Eric D. Walter<sup>2</sup>, Nancy M. Washton<sup>2</sup>, Donghai Mei<sup>1</sup>, Tamas Varga<sup>2</sup>, Yilin Wang<sup>1</sup>, János Szanyi<sup>1</sup>, Yong Wang<sup>1</sup>, Charles H.F. Peden<sup>1</sup> & Feng Gao<sup>1</sup>

Commercial Cu/SAPO-34 selective catalytic reduction (SCR) catalysts have experienced unexpected and quite perplexing failure. Understanding the causes at an atomic level is vital for the synthesis of more robust Cu/SAPO-34 catalysts. Here we show, via application of model catalysts with homogeneously dispersed isolated Cu ions, that Cu transformations resulting from low-temperature hydrothermal aging and ambient temperature storage can be semi-quantitatively probed with 2-dimensional pulsed electron paramagnetic resonance. Coupled with kinetics, additional material characterizations and DFT simulations, we propose the following catalyst deactivation steps: (1) detachment of Cu(II) ions from cationic positions in the form of Cu(OH)<sub>2</sub>; (2) irreversible hydrolysis of the SAPO-34 framework forming terminal Al species; and (3) interaction between Cu(OH)<sub>2</sub> and terminal Al species forming SCR inactive, Cu-aluminate like species. Especially significant is that these reactions are greatly facilitated by condensed water molecules under wet ambient conditions, causing low temperature failure of the commercial Cu/SAPO-34 catalysts.

<sup>1</sup>Institute for Integrated Catalysis, Pacific Northwest National Laboratory, P.O. Box 999, Richland, WA 99354, USA. <sup>2</sup>Environmental Molecular Sciences Laboratory, Pacific Northwest National Laboratory, P.O. Box 999, Richland, WA 99354, USA. Correspondence and requests for materials should be addressed to E.D.W. (email: [eric.walter@pnnl.gov](mailto:eric.walter@pnnl.gov)) or to D.M. (email: [donghai.mei@pnnl.gov](mailto:donghai.mei@pnnl.gov)) or to F.G. (email: [feng.gao@pnnl.gov](mailto:feng.gao@pnnl.gov))

The commercialization of hydrothermally robust, copper-exchanged small pore molecular sieve materials, Cu/SSZ-13 and Cu/SAPO-34, as selective catalytic reduction (SCR) catalysts for diesel engine exhaust aftertreatment, has been a major milestone in environmental catalysis in recent years<sup>1–3</sup>. Approaching the end of the first decade of commercial use, however, these two catalysts are now facing significantly different fates. While Cu/SSZ-13 continues to provide satisfactory performance, Cu/SAPO-34 is gradually retreating from the market due to performance failures. This was unexpected in light of the fact that Cu/SAPO-34 has been repeatedly found to be more stable than Cu/SSZ-13 during accelerated high-temperature (>700 °C) hydrothermal aging<sup>4–6</sup>, which generally translates to better long-term stability for a SCR catalyst.

Recent investigations indicate that Cu/SAPO-34 lacks durability at low temperatures (<100 °C) in the presence of moisture, with causes that are still not clearly understood<sup>6–8</sup>. Through our own investigations with the current state-of-the-art Cu/SAPO-34 catalysts, and from recent literature reports<sup>6,7</sup>, the unexpected low-temperature Cu/SAPO-34 catalyst failure has specific attributes. In particular, a heavily deactivated catalyst can still maintain considerable Chabazite structural integrity as determined from X-ray diffraction (XRD), suggesting that structural degradation of the SAPO-34 support alone, due to well-established irreversible hydrolysis<sup>9</sup>, cannot, by itself, explain catalyst failure. Rather, the transformation of SCR active Cu species into inactive ones appears to be a more plausible explanation<sup>7</sup>. However, it is not clear at all how such transformations occur at near-ambient conditions.

Although understanding low-temperature instability of Cu/SAPO-34 is critical for designing more robust SCR catalysts, explicit causes are difficult to identify, because of the intrinsic structural complexity of such catalysts. First, SAPO-34 can be synthesized using a wide variety of Al/P/Si precursors and structure directing agents (SDAs), forming SAPO-34 materials with different T-site distributions and thus, different sensitivities to moisture<sup>9,10</sup>. Second, Cu distributions can be highly complex<sup>6,11–13</sup>. Solution ion exchange, the commonly used method for the synthesis of Cu/SAPO-34 catalysts, inevitably leads to the coexistence of preferred isolated Cu ions and unwanted CuO, as well as uneven Cu distributions within individual SAPO-34 particles<sup>11,12</sup>. This complexity renders Cu transformations under varying hydrothermal treatments difficult to trace and quantify.

To circumvent catalyst complexity described above, a one-pot synthesis approach was applied here to prepare model Cu/SAPO-34 catalysts with uniformly dispersed Cu species that are essentially present as isolated ions at cationic sites (i.e., the SCR active form). To speed up low-temperature hydrolysis of these model catalysts, morpholine was chosen as the primary SDA, which is known to lead to SAPO-34 materials more vulnerable to water attack than with other common SDAs<sup>9</sup>. Atomic Cu dispersion was achieved by using Cu-TEPA (tetraethylenepentamine) complexes as the Cu source, a species that is stable during one-pot synthesis and can also function as a co-SDA<sup>14,15</sup>. By varying the amount of Cu-TEPA, two samples with Cu loadings of 0.71 wt% (Cu1) and 1.90% (Cu2) were synthesized. Details on the compositions of the two catalysts are provided in Table S1. The freshly prepared, dried and calcined samples (designated as “F”) were divided into two parts, one being treated hydrothermally either at 70 °C (designated as “LT”) or 800 °C (“HT”), and second being stored in a typical ambient lab environment (~20 °C, relative humidity ~50%) for 240 days (“S”).

In the main body of the current work, these catalysts are analyzed with a number of spectroscopic and chemical titration methods to elucidate structural changes in SAPO-34 and Cu transformations. The observed structural modifications are then

correlated with catalytic performance in the standard NH<sub>3</sub> SCR reaction (4NO+4NH<sub>3</sub>+O<sub>2</sub>=4N<sub>2</sub>+6H<sub>2</sub>O). In particular, hyperfine sublevel correlation (HYSCORE) spectroscopy, a two-dimensional (2D) pulsed electron paramagnetic resonance (EPR) technique<sup>16</sup>, is used to gain important insight on Cu transformations. The experimental studies are then closely coupled with detailed density functional theory calculation to unravel the underlining destructive mechanism by water which only occurs below 100 °C.

## Results and discussion

**Effects on standard SCR performance.** Standard SCR testing was conducted at a few space velocities to measure light-off behaviors and turnover rates under kinetic control<sup>17</sup>. Supplementary Fig. 1a, b presents light-off curves of Cu1 and Cu2 samples in F, LT, and HT forms. For Cu1, both low- and high-temperature hydrothermal treatments induce remarkable deactivation. For Cu2, low (<~200 °C) temperature NO<sub>x</sub> conversions decrease with hydrothermal treatments; yet catalytic performance is maintained (for Cu2-HT) or even enhanced (for Cu2-LT) at higher reaction temperatures. SCR performance of the Cu1-S sample stored under ambient conditions was unexpected. As shown in Supplementary Fig. 2, at reaction temperatures where Cu1-F reaches ~100% NO<sub>x</sub> conversions, Cu1-S only shows NO<sub>x</sub> conversions lower than ~20%. Furthermore, this catalyst becomes less selective in SCR above ~400 °C as indicated by the striking differences between NO<sub>x</sub> and NH<sub>3</sub> conversions. As will be shown below, however, this sample is much more informative in revealing low-temperature deactivation mechanisms for Cu/SAPO-34 than any other samples studied here. In particular, The Cu2-S sample (not shown), on the other hand, displays essentially identical catalytic performance as Cu2-LT and, as such, was not further explored in this study.

To obtain more details on the effects of Cu transformations on SCR performance, standard SCR reactivity was also measured under kinetic control (i.e., at low-temperature differential conditions). In this way, turnover frequencies (TOFs) could be calculated assuming that SCR is catalyzed by isolated Cu(II) ions, with the latter quantified using electron paramagnetic resonance (EPR) analysis of hydrated ambient samples (as described below)<sup>17</sup>. Fig. 1a presents TOFs of the Cu1 samples in the form of Arrhenius plots. Cu1-F/LT/HT samples display essentially identical apparent activation energies (93 ± 1 kJ/mol), typical for NH<sub>3</sub>-SCR over Cu/zeolites under kinetic control (i.e., at low conversions in the absence of mass transfer limitations)<sup>17,18</sup>. Similarity in activation energies indicates active sites of the same nature in different samples; however, TOFs for the Cu1-LT sample are ~56% lower than that over Cu1-F, whereas TOFs for Cu1-HT are only ~8% lower than that on Cu1-F. This indicates that a large portion of EPR active isolated Cu(II) species in Cu1-LT are not SCR active, causing the decrease of the apparent TOFs, since these are normalized against total EPR active Cu(II) sites. The Cu1-S sample, in contrast, not only displays substantially lower reactivity even in comparison to Cu1-LT, but also a significantly lower apparent activation energy, suggesting that the nature of active site has been altered. Figure 1b presents the corresponding Arrhenius plots for the Cu2 samples. Again, similar apparent activation energies of 96.5 ± 2.5 kJ/mol are obtained demonstrating kinetic control, and suggesting similar active sites in each of these samples. In comparison to Cu2-F, the Cu2-LT sample experienced larger TOF drop (~26%) than the Cu2-HT sample (~6%). This is consistent with Cu1, where low-temperature hydrothermal aging causes more significant activity loss. It is important to note that the rate losses described above are caused by the water treatments prior to SCR

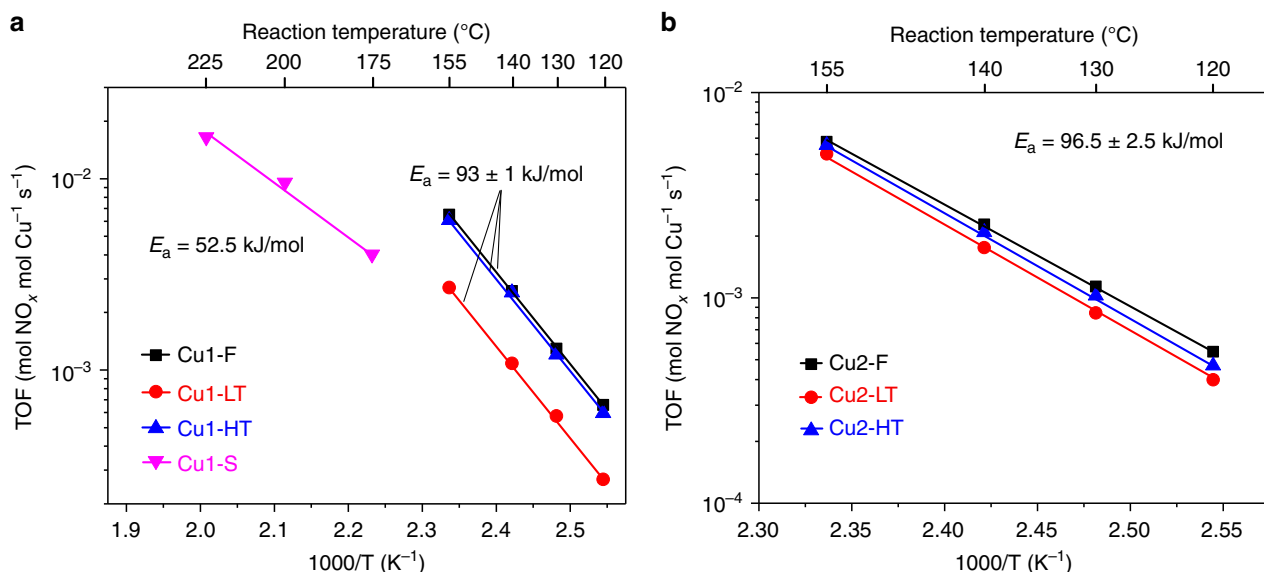


**Fig. 1** Arrhenius plots for low-temperature standard NH<sub>3</sub>-SCR. **a** Cu1-F/LT/HT catalysts; **b** Cu2-F/LT/HT catalysts. The feed gas contained 360 ppm NO, 360 ppm NH<sub>3</sub>, 14% O<sub>2</sub>, 2.5% H<sub>2</sub>O and balance N<sub>2</sub>. The total gas flow was 1000 sccm, and the gas hourly space velocity (GHSV) was estimated to be ~650,000 h<sup>-1</sup>. TOFs were calculated using EPR active Cu(II) contents in each sample

tests. During the short SCR tests, no catalyst deactivation has been observed.

**Textural property analyses and chemical titrations.** Multiple standard materials characterizations were performed on the catalysts studied here. In particular, surface area/pore volume and XRD analyses were used to reveal crystallinity changes, temperature-programmed desorption of ammonia (NH<sub>3</sub>-TPD) was applied to probe NH<sub>3</sub> storage capacity, and temperature-programmed reduction with hydrogen (H<sub>2</sub>-TPR) was used to study Cu ion reduction characteristics. Isolated Cu(II) ion concentrations were measured by double-integrating EPR signals of fully hydrated samples, and quantification was made using solution Cu-imide complexes with known concentrations. Most of the results are collectively shown in Table 1; more detailed descriptions and discussions are presented in Supplementary Figs. 3–6. In brief, these results support the structure-stabilizing role for Cu ions discovered recently<sup>8</sup>, and demonstrate that low- and high-temperature hydrothermal aging have very different effects on the nature of Cu species present in the catalysts. For the Cu1-S sample in particular, in situ XRD during dehydration demonstrates that, while this sample maintains the Chabazite structural integrity in the fully hydrated ambient form, even a very mild thermal treatment causes the structure to collapse indicative of the highly defective nature for this sample (Supplementary Fig. 3b). Next, focus will be given to the transformations of Cu in the Cu1 samples from detailed EPR analyses.

**Cu transformations via 1D and 2D EPR.** Supplementary Fig. 7 presents 1D continuous wave (CW) EPR spectra of the hydrated Cu1 samples. In addition to signal amplitude variation, the hyperfine features (enlarged as an insert) also display considerable differences among the samples. From these spectra,  $g_{||}$  and  $A_{||}$  tensor values were derived and the results are tabulated in Supplementary Table 2. The amounts of EPR active Cu contents were also included in the table. As shown above, the Chabazite structure of the Cu1-S sample collapses during dehydration. Therefore, EPR spectra of the dehydrated Cu1-F and Cu1-S samples were acquired to reveal their differences, and the results are shown in Supplementary Fig. 8. Interestingly, the high-field

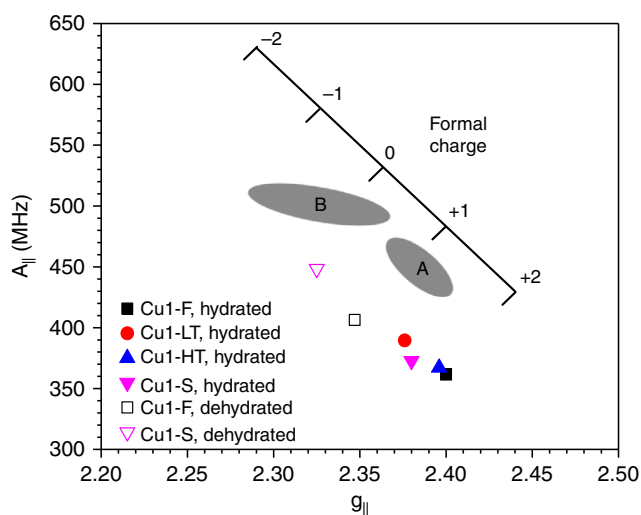
signal appears to split into two features (apparent  $g$  factors  $g' = 2.050$  and  $2.035$ ) for the dehydrated Cu1-S sample. Again, total EPR active Cu contents and  $g_{||}$  and  $A_{||}$  tensor values were obtained and these are displayed in Supplementary Table 2. Upon structural collapse, even though the majority of Cu species (~56%) remain as isolated Cu(II), the nature of Cu in this sample is very different from other samples as evidenced from H<sub>2</sub>-TPR (Supplementary Fig. 6), and from SCR test (Fig. 1).

In a classic study by Carl and Larsen<sup>19</sup>,  $g_{||}$  and  $A_{||}$  tensors for Cu(II) ions in varied zeolites (in both hydrated and dehydrated forms) were summarized, and a correlation between the formal charge on Cu(II) and these EPR parameters was established. As shown in Fig. 2,  $g_{||}$  and  $A_{||}$  tensor pairs are typically found in shaded area A for hydrated Cu(II) ions with a formal charge close to +1. Upon dehydration,  $g_{||}$  and  $A_{||}$  tensor pairs are typically found in shaded area B, i.e.,  $A_{||}$  increases, whereas  $g_{||}$  and formal charge decrease, as a result of stronger Cu(II)-support interactions. For the Cu1 samples studied here, the  $g_{||}$  and  $A_{||}$  tensor pairs are also plotted in Fig. 2. In comparison to other Cu/zeolites,  $A_{||}$  tensor values for our Cu/SAPO-34 samples are considerably lower indicating weaker Cu-support interactions for the latter. In the hydrated form, Cu1-F and Cu1-HT display very similar Cu-support interactions suggesting that high-temperature treatment does not alter the nature of Cu in hydrated samples, whereas both hydrothermal treatment at 70 °C and ambient temperature storage enhance Cu-support interactions, suggesting differences in the nature of Cu sites as opposed to the fresh sample. For the dehydrated Cu1-F and Cu1-S samples, again, the large differences in  $g_{||}$  and  $A_{||}$  tensor values and “formal” Cu charges indicate the different nature of Cu species in the two samples.

Next, 2D pulsed EPR (HYSCORE) was applied to further elucidate changes to the local environments of the Cu(II) species in low/high-temperature aging and in room temperature storage. Note that this technique probes interactions between an unpaired electron in Cu(II) and nearby NMR-active nuclei (<sup>27</sup>Al, <sup>1</sup>H for this system), with an effective range of 0.25–0.8 nm. Figure 3 presents contour spectra for the four hydrated samples normalized with experimental signal intensity/videogain/mass. These spectra are replotted in Supplementary Fig. 9 as surface plots to visually assist spectra comparisons for Fig. 3. Note that each spectrum contains two quadrants. The majority of signals appear

**Table 1** Textural properties, chemical titration results, and isolated Cu(II) contents of the catalysts

Sample	BET surface area (m <sup>2</sup> /g) <sup>a</sup>	Micropore volume (cm <sup>3</sup> /g) <sup>a</sup>	NH <sub>3</sub> storage (mmol/g) <sup>b</sup>	H/Cu ratio (100–600 °C) <sup>c</sup>	EPR active Cu (wt %)
Cu1-F	364	0.204	0.825	1.63 ± 0.16	0.70
Cu1-LT	208	0.112	0.577	1.84 ± 0.12	0.67
Cu1-HT	184	0.097	0.314	1.18 ± 0.05	0.60
Cu1-S	86	0.042	0.114	1.98 ± 0.08	0.51
Cu2-F	456	0.241	0.874	1.65 ± 0.04	1.63
Cu2-LT	344	0.189	0.886	1.68 ± 0.09	1.42
Cu2-HT	390	0.210	0.804	1.78 ± 0.08	1.48

<sup>a</sup>Measured with N<sub>2</sub> adsorption<sup>b</sup>Measured with NH<sub>3</sub>-TPD<sup>c</sup>Measured with H<sub>2</sub>-TPR**Fig. 2** Correlations between ( $g_{||}$ ,  $a_{||}$ ) tensor pairs and formal charges of Cu(II) ions in the Cu1 samples. Note that shaded areas “A” and “B” represent typical ( $g_{||}$ ,  $A_{||}$ ) pair positions found in hydrated and dehydrated Cu/zeolite materials, respectively

in the right (+, +) quadrant, symmetrical along the diagonal. There are some signals that appear in the left (–, +) quadrant, which many times indicates very strong coupling<sup>20</sup>. Note also that signal splitting from the diagonal reflects the strength of coupling between the electron and the nuclei that couples with it: narrow peaks that fall on the diagonals come from nuclei at longer distances; off-diagonal signals originate from strong coupling indicating shorter distances.

For the Cu1-F sample, two groups of features are observed in the (+, +) quadrant: features at lower frequencies are attributed to <sup>27</sup>Al coupled with Cu(II); features at high frequencies to <sup>1</sup>H. The strong coupling between Cu(II) and <sup>1</sup>H indicates that a large portion of isolated Cu(II) sites in this catalyst stays as [Cu(OH)]<sup>+</sup>, one of the two active forms of Cu ions found in the isostructural Cu/SSZ-13 catalysts<sup>3</sup>. For the Cu1-LT catalyst, the <sup>1</sup>H features appear similar to, but somewhat weaker than Cu1-F, indicating large preservation yet some consumption of Cu–OH bonds. For Cu1-HT, Cu–<sup>1</sup>H coupling becomes much lower in intensity compared with that in Cu1-F and Cu1-LT, indicating substantial consumption of Cu–OH. In comparison to Cu1-F, Cu(II)–<sup>27</sup>Al coupling becomes weaker in the (+, +) quadrant, yet slightly more intensive in the (–, +) quadrant for Cu1-LT. In contrast, Cu(II)–<sup>27</sup>Al coupling for Cu1-HT in both quadrants becomes stronger than Cu1-F. In

particular, the near-diagonal signal splits into two features in the (+, +) quadrant, indicating very strong Al–Cu–Al interactions (Fig. 9). HYSCORE simulations (detailed in Supplementary Figs. 10–14) indicate that these strongly coupled <sup>27</sup>Al nuclei are at a distance of ~2.7 Å, with the features in the (–, +) quadrant that are best simulated with two <sup>27</sup>Al nuclei rather than one (i.e., with –Al–O–Cu–O–Al– configurations)<sup>21</sup>. The following reaction, i.e., [Cu(OH)]<sup>+</sup> + H<sup>+</sup> = Cu<sup>2+</sup> + H<sub>2</sub>O, best describes high-temperature Cu transformation, which converts thermodynamically less stable [Cu(OH)]<sup>+</sup> to more stable Cu<sup>2+</sup> that has been found to occur also in Cu/SSZ-13 during high-temperature hydrothermal aging<sup>18,22</sup>. Note that this transformation does not alter SCR activity since both isolated sites have roughly equal SCR activity (Fig. 1)<sup>23</sup>.

The HYSCORE spectrum of the Cu1-S sample displays a number of surprising features. First, the <sup>1</sup>H signals are very weak, indicating that the majority of [Cu(OH)]<sup>+</sup> converts to other species. However, at ambient temperatures and with CHA pores filled with trapped H<sub>2</sub>O, detachment of –OH groups from Cu ions is not readily rationalized. The <sup>27</sup>Al signals are also an order of magnitude lower than other samples. Note that hydrated Cu(II) ions in CHA cages can couple effectively with framework Al sites (within effective coupling distances of 0.25–0.8 nm). The decreased Cu–Al coupling, therefore, may indicate that a large portion of Cu(II) species are no longer present at cationic exchange positions. In other words, Cu(II) species have migrated a considerable distance from the exchange sites and, therefore, couple few Al sites in the Cu1-S sample.

**<sup>27</sup>Al, <sup>29</sup>Si, and <sup>31</sup>P solid-state NMR.** As clearly shown from the EPR analyses, ambient temperature storage induces considerable changes to bonding and locations of Cu ions. Such changes seem likely due, at least in part, to a modified structure of the SAPO-34 zeolite during storage which is not readily captured with XRD (Supplementary Fig. 3). In the following, solid-state NMR was applied to compare Cu1-F and Cu1-S in both hydrated and dehydrated forms. Supplementary Figs. 15a–c present direct polarization (DP) <sup>27</sup>Al, <sup>29</sup>Si, and <sup>31</sup>P spectra for hydrated Cu1-F and Cu1-S samples, together with detailed peak assignments and descriptions. In brief, these spectra collectively demonstrate a much more defective nature for Cu1-S, as evidenced by the higher concentrations of distorted and/or hydrated T sites (even though the Chabazite structure maintains). Supplementary Fig. 16a, b present <sup>27</sup>Al and <sup>31</sup>P direct polarization (DP) and cross polarization (CP, with <sup>1</sup>H) spectra of dehydrated Cu1-F and Cu1-S samples, respectively (in this case, the Chabazite structure collapses for Cu1-S). Again, some descriptions are also presented to further demonstrate the strong coupling between defective Al and H in close vicinity (–OH or strongly bound H<sub>2</sub>O) even after Chabazite structure collapse. In contrast, –OH or strongly bound H<sub>2</sub>O shows much less interaction with P species in the zeolite.

**The nature of Cu–Al interactions below 100 °C.** The results shown above, especially EPR and NMR analyses of the Cu1-S and Cu1-LT samples, demonstrate dramatic Cu transformations from the SCR active form (i.e., isolated Cu-ions in cationic positions) to an SCR inactive, but still EPR detectable form (i.e., still as isolated Cu(II)). H<sub>2</sub>-TPR results shown in Supplementary Fig. 6 provide important indications on the nature of the latter Cu moieties. For the Cu1-S sample, reduction centered at ~365 °C is readily assigned to Cu(II) → Cu(0) reduction based on the H/Cu quantification. Moreover, the rather high reduction temperature suggests that the Cu moieties in this sample are clearly no longer isolated Cu(II)



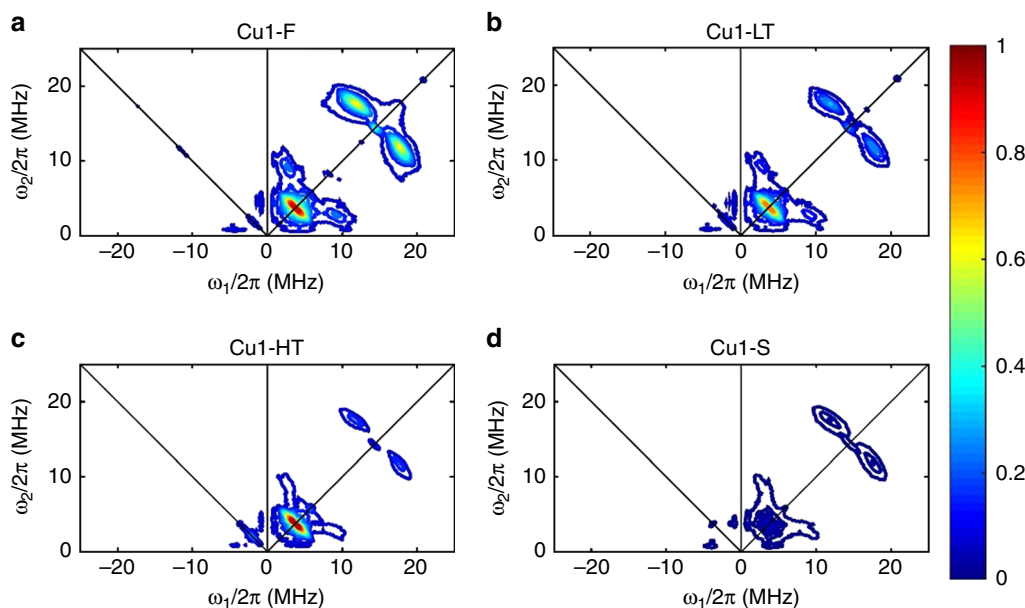


**Fig. 3** HYSORE spectra for hydrated CuI samples. **a** Cu1-F; **b** Cu1-LT; **c** Cu1-HT; **d** Cu1-S. The four spectra have undergone normalization to signal intensity/video gain/mass, using the same color scale and contour level for the purpose of direct comparison

ions in zeolite cationic positions which are reduced to Cu(I) at much lower temperatures. Rather, the reduction temperature matches very well with reduction of copper aluminate-like species generated during hydrothermal treatment of Cu/zeolites<sup>24</sup>. To elucidate whether Cu-aluminate-like species form in Cu1-S, a physical mixture of CuO and  $\gamma$ -Al<sub>2</sub>O<sub>3</sub> (containing 1 wt% Cu) was calcined in air at 1000 and 1200 °C, and then subjected to EPR analyses. As shown in Supplementary Fig. 17a, the sample calcined at 1000 °C contains 0.31 wt% EPR active Cu, suggesting formation of CuAl<sub>2</sub>O<sub>4</sub> with EPR active Cu (II). In contrast, the sample calcined at 1200 °C only contains 0.03 wt% EPR active Cu, suggesting dominance of CuAlO<sub>2</sub> in which Cu has a +1 oxidation state and is, thus, EPR silent. Importantly, the sample calcined at 1000 °C after dehydration also displays two features in the high field with apparent *g*' = 2.050 and 2.031 as shown in Supplementary Fig. 17b. Even though the nature of the two high-field features awaits further elucidation, the similarity between this spectrum and that of the dehydrated Cu1-S sample (Supplementary Fig. 8) strongly suggests formation of Cu-aluminate-like species in the Cu/SAPO-34 sample stored under ambient conditions for nearly a year. In fact, from XRD, HYSORE and <sup>29</sup>Si NMR results, strong Cu–Al interactions even occur at ambient temperatures without appreciable destruction of the Chabazite structure; i.e., before extensive desilication of the SAPO-34 substrate occurs. This is believed to be the main reason why a deactivated industrial catalyst still appears “normal” in terms of structural integrity.

Formation of CuAl<sub>2</sub>O<sub>4</sub>-like species requires (1) formation of reactive terminal  $\equiv\text{Al}-\text{OH}/\equiv\text{Al}(\text{H}_2\text{O})_n$  ( $n = 1-3$ ) via hydrolysis of the SAPO-34 substrate<sup>9,25</sup>, and (2) transformation of SCR active Cu(II) ions in cationic positions to Cu moieties that can react with  $\equiv\text{Al}-\text{OH}/\equiv\text{Al}(\text{H}_2\text{O})_n$  to form CuAl<sub>2</sub>O<sub>4</sub>-like species, or at least its precursors. We have recently shown that [Cu(OH)]<sup>+</sup> active sites can detach from cationic positions via a hydrolysis chemistry<sup>18,22</sup>, i.e., [Cu(OH)]<sup>+</sup> + H<sub>2</sub>O = Cu(OH)<sub>2</sub> + H<sup>+</sup>. This reaction leads to the formation of free Cu(OH)<sub>2</sub> molecules and regeneration of Brønsted acid sites ( $\equiv\text{Si}-\text{O}(\text{H})-\text{Al}\equiv$ ) that are vulnerable to hydrolysis. Unlike zeolites that dealuminate during hydrothermal treatment,

desilication is more facile for SAPO materials<sup>25</sup>. Upon sequential hydrolysis of  $\equiv\text{Si}-\text{O}(\text{H})-\text{Al}\equiv$  bonds, free Si(OH)<sub>4</sub> and terminal  $\equiv\text{Al}-\text{OH}/\equiv\text{Al}(\text{H}_2\text{O})_n$  moieties form. In the following, we describe theoretical approaches that were used to gain atomic-level details of these chemistries, particularly why these only occur at near-ambient temperatures (<100 °C).

Here, we simulate how (condensed) water promotes [Cu(OH)]<sup>+</sup> hydrolysis to Cu(OH)<sub>2</sub>,  $\equiv\text{Si}-\text{O}(\text{H})-\text{Al}\equiv$  hydrolysis, and interactions between Cu(OH)<sub>2</sub> and terminal Al species. A model Cu/SAPO-34 structure was constructed that contains two hexagonal unit cells (72 T) with Si/P/Al = 1/2/3. The optimized simulation cell parameters are 13.6433 × 23.6310 × 14.8205 Å<sup>3</sup>. One [Cu(OH)]<sup>+</sup> was used to replace a proton in an 8-membered ring as the reactive site. This structure is simple enough for simulation purposes, and mimics the Cu1 sample composition rather well. As shown in Supplementary Fig. 18, the DFT calculated Cu–Al and Cu–H distances for the optimized structure, 2.86 and 2.37 Å, respectively, are very close to values obtained via HYSORE simulations (2.74 and 2.48 Å, respectively), thus validating the representativeness of our structural model.

Given the hydrophobic nature of silicoaluminophosphate zeotype materials<sup>11</sup>, water adsorption by Cu/SAPO-34 must be associated with Brønsted acid sites, Cu-ions and other minor defect sites. At low Cu loadings (e.g., Cu1), Brønsted acid sites are considered as the main contributor for H<sub>2</sub>O adsorption. As such, the numbers of water molecules that can be stabilized by Brønsted acid sites as a function of temperature at 1 bar is first simulated. As shown in Supplementary Fig. 19, each Brønsted acid site can accommodate up to ~10 water molecules at 0 K. With increasing temperature or the number of water molecules, neighboring Brønsted acid sites will be involved for their stabilization. Figure 4 presents the calculated Gibbs free adsorption energies<sup>26</sup> of varying numbers of water molecules in the vicinity of each Brønsted acid site as a function of temperature. It is readily deduced from this simulation that ~3–5 water molecules can be stabilized in the vicinity of each Brønsted acid site at temperatures below 100 °C. From the catalyst compositions shown in Supplementary Table 1, and Si distributions from Supplementary Fig. 15b (note that silica

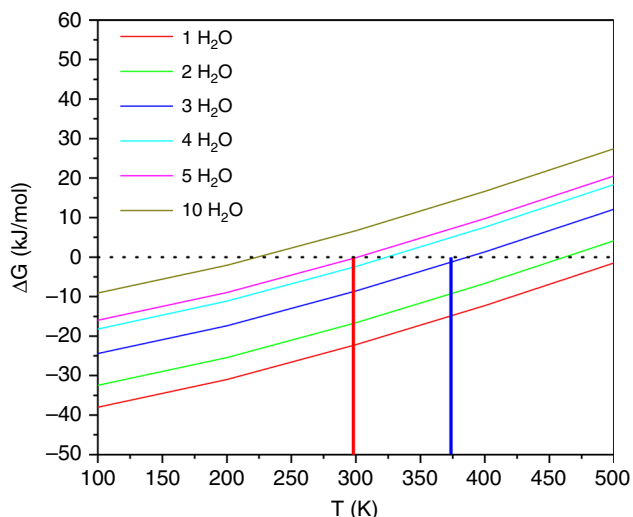


**Fig. 4** Calculated Gibbs free adsorption energies as a function of temperature. The 6 thin solid curves describe scenarios with different number of H<sub>2</sub>O molecules (1–10) in the vicinity of a Brønsted acid site. The dashed horizontal line represents Gibbs free energy at zero, and the vertical red and blue lines correspond to 298 K and 373 K, respectively

islands do not provide Brønsted acidity<sup>10,27</sup>), it is estimated that each hexagonal unit cell contains ~2–3 Brønsted acid sites. This translates to the availability of ~6–15 water molecules in each unit cell for the hydrolysis chemistries described above. Such estimations can be readily verified experimentally. Desorption of 15 H<sub>2</sub>O molecules from one unit cell corresponds to ~10% weight loss; this value is consistent with typical weight losses of ~10–20% in Cu/SAPO-34 dehydration. Next, it will be shown that the strong solvation effects provided by multiple water molecules and occurring only below 100 °C, play a decisive role in promoting (1) [Cu(OH)]<sup>+</sup> hydrolysis to free Cu(OH)<sub>2</sub>, (2) ≡Si-O(H)-Al≡ hydrolysis to terminal reactive Al, and (3) Cu(OH)<sub>2</sub> and terminal Al interactions. At elevated temperatures (e.g., 800 °C), water concentrations within the SAPO-34 cages are negligible, thus precluding such reactions.

Figure 5 presents Gibbs free energy diagrams of [Cu(OH)]<sup>+</sup> cationic site hydrolysis to free Cu(OH)<sub>2</sub> and H<sup>+</sup> in the presence of 1, 3, and 5 water molecules. In considerable contrast to a high barrier of 136 kJ/mol when only 1 H<sub>2</sub>O molecule participates in the hydrolysis, the activation barrier for the formation of Cu(OH)<sub>2</sub> decreases from 34 kJ/mol with 3 water molecules to 6 kJ/mol for 5 water molecules in the vicinity of Cu. The optimized structures of the intermediate states are given in Supplementary Fig. 20. As suggested by previous experimental work<sup>28,29</sup>, the hydrolysis of ≡Si-O(H)-Al≡ and ≡P-O-Al≡ bonds in SAPO-34 leads to formation of terminal Al sites. Our calculations show that the hydrolysis of ≡P-O-Al≡ bonds is highly endothermic under the relevant water concentrations studied here. In contrast, the hydrolysis of ≡Si-O(H)-Al≡ bonds is facile. Previous NMR studies<sup>9,28</sup> suggest that the hydrolysis chemistry can be depicted as follows: ≡Si-O(H)-Al≡ + 3H<sub>2</sub>O = ≡Si-OH + ≡Al(H<sub>2</sub>O)<sub>3</sub>. As shown in Supplementary Fig. 21, in the presence of 2 extra H<sub>2</sub>O molecules, the activation barrier drops significantly from 69 to 31 kJ/mol, and the entire hydrolysis process also changes from slightly endothermic to exothermic.

Finally, interactions between ≡Al(H<sub>2</sub>O)<sub>3</sub> and Cu(OH)<sub>2</sub> (for the formation of a precursor to CuAl<sub>2</sub>O<sub>4</sub>) are simulated. As shown in Supplementary Fig. 22, without the participation of extra water molecules, complexing the two moieties requires a rather high activation barrier of 73 kJ/mol due to repulsion between the two, and the final formation of =Al(μ-O<sub>2</sub>)Cu (a precursor to

CuAl<sub>2</sub>O<sub>4</sub>) is endothermic with respect to the initial state. However, when two extra H<sub>2</sub>O molecules are used to solvate Cu(OH)<sub>2</sub>, the activation barrier drops to 15 kJ/mol, and the entire process becomes exothermic. The preceding simulations, intended to be illustrative rather than exhaustive (for example, ≡Al-OH formation and its interactions with Cu(OH)<sub>2</sub> are not simulated here) because detailed CuAl<sub>2</sub>O<sub>4</sub> formation pathways are still not clear, do point to the same general conclusion that the presence of multiple water molecules, a more likely scenario at relatively low temperatures, plays a crucial and beneficial role in lowering barriers for the chemistries that lead to the formation of this species.

**Implications to industrial applications.** The transportation industry has been puzzled by the slow but irreversible deactivation of Cu/SAPO-34 SCR catalysts for some time in that, despite catalytic performance loss, a deactivated catalyst is otherwise “normal” in comparison to a fresh one as characterized by many standard methods<sup>6,7</sup>. For the Cu<sub>2</sub> sample studied here (which has a composition similar to industrial catalysts), indeed, because of its relatively high stability and complexity in Cu identity and distribution, activity loss during low-temperature hydrothermal treatment is difficult to explain. Using our specifically prepared Cu<sub>1</sub> sample with uniform Cu distribution and almost singular Cu identity, for the first time, we are able to at least semi-quantitatively follow Cu transformations from SCR active to inactive forms via 1D and 2D EPR. This study is yet another example of utilizing relevant but simplified model catalysts to unambiguously pinpoint key aspects of catalytic processes (in this case deactivation). The most important finding here is that chemistries associated with catalyst deactivation, including structural degradation of the SAPO-34 support and transformation of Cu sites, are greatly facilitated by condensed water within catalyst cages.

Improvements in catalyst design, e.g., by optimizing Si distributions, as well as Cu loadings and distributions, can be used to increase stability of Cu/SAPO-34 catalysts as others have also proposed<sup>15</sup>. In the work by Wang et al.<sup>8</sup>, the authors discovered that Cu/SAPO-34 catalysts free from low-temperature water attack contain saturated amounts of ~2.2 wt% isolated Cu(II) ions as determined via EPR. Such loadings correspond to ~1 isolated Cu(II) ion per hexagonal unit cell. This suggests that: (1) repulsive interactions between mobile water-solvated Cu(II) ions preclude the coexistence of more than one such ions in each unit cell; (2) when each unit cell contains one such isolated Cu(II) ion, it is well protected from low-temperature water attack. Our Cu<sub>1</sub>-F sample contains an isolated Cu(II) loading of 0.7 wt%, corresponding to one Cu(II) ion in every 4 unit cells, i.e., 3 of 4 unit cells are unprotected from low-temperature water attack. It can be anticipated that unit cells without Cu(II) protection will deform first (not necessarily collapse since the pores are filled with water) from low-temperature water attack, leaving unit cells containing Cu(II) also more vulnerable to water attack. Therefore, the rule that one hexagonal unit cell containing one isolated Cu(II) ion can be used as a guideline for the synthesis of stable Cu/SAPO-34 catalysts. Findings from the current study suggest further that the most important criterion in preventing deactivation of Cu/SAPO-34 catalysts is to prevent the hydrolysis chemistries of ≡Si-O(H)-Al≡ and [Cu(OH)]<sup>+</sup> sites from occurring at low temperatures. This could be achieved, for example, by flushing the SCR catalyst bed with ammonia, the only SCR relevant molecule that binds more strongly with these sites than H<sub>2</sub>O, thus suppressing H<sub>2</sub>O induced hydrolysis when the catalyst bed temperature decreases to ~100 °C. Our Cu<sub>1</sub> catalyst saturated with ammonia indeed shows no sign of deactivation following the same 8-month shelf

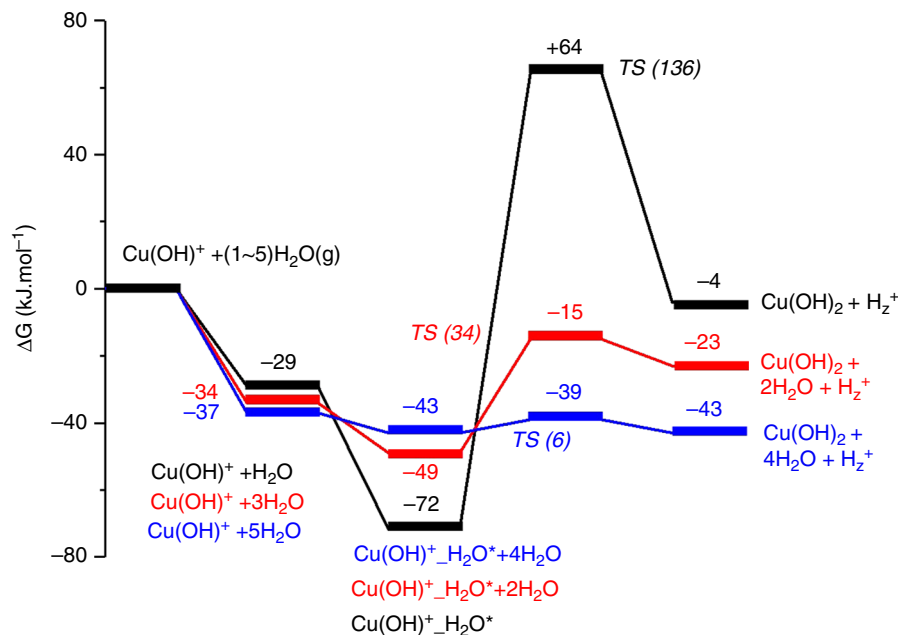


**Fig. 5** The effects of water concentration on the hydrolysis of the  $[\text{Cu}^{\text{II}}(\text{OH})]^+$  to  $\text{Cu}(\text{OH})_2$ . Optimized structures of each intermediates are given in Supplementary Fig. 20

storage treatment, clearly demonstrating the protective role of ammonia in preventing water damage.

To summarize, using model Cu/SAPO-34 catalysts with homogeneously dispersed and isolated Cu ions, Cu species transformations and SAPO-34 structural degradation were investigated using SCR kinetics, spectroscopy (in particular, EPR and NMR), and DFT simulations. These results for the first time provide a satisfactory explanation for the unusual failure of commercial Cu/SAPO-34 SCR catalysts. Hydrolysis chemistries lead to detachment of isolated Cu ions from CHA cationic positions and concurrent formation of terminal Al sites; reactions between these latter moieties generate SCR inactive Cu-aluminate like species. While optimizing catalyst compositions (Si distribution, Cu loading, etc.) will increase durability of this catalyst, a simple yet practical modification of catalyst pretreatment strategies, e.g. via saturation ammonia adsorption, can effectively prevent the low-temperature hydrolysis of Cu active centers and Brønsted acid sites, providing a useful solution to this important practical problem.

## Methods

**Catalyst preparation and treatment.** One-pot Cu/SAPO-34 catalysts presented in this study were synthesized using a method similar to that used by Prakash and Unnikrishnan<sup>30</sup> for the synthesis of pure SAPO-34, except for Cu addition into the gel for the current case. A Cu-TEPA complex solution, prepared by mixing 5 g of anhydrous  $\text{CuSO}_4$ , 6 g of tetraethylenepentamine (TEPA) and 89 g of d.i. water, was used as the Cu source. This complex has been shown to be stable during SAPO-34 synthesis, which also serves as a co-structure directing agent (co-SDA)<sup>15,31</sup>. Morpholine (MOR) was chosen as the primary SDA. Previous studies have shown that this SDA leads to SAPO-34 materials relatively vulnerable to water attack<sup>6,9</sup>. This characteristic is not ideal for applications, but benefited this study of Cu/SAPO-34 degradation. 85% o-phosphoric acid ( $\text{H}_3\text{PO}_4$ ) was used as the P source; aluminum hydroxide powder (containing ~54%  $\text{Al}_2\text{O}_3$ ) was used as the Al source, and fumed silica (0.001  $\mu\text{m}$  particle size) was used as the Si source. All chemicals used in our syntheses were purchased from Sigma-Aldrich with purities of analytical grade or better. Synthesis gel molar composition was the following: 0.038 or 0.114 Cu-TEPA: 2 MOR: 0.9  $\text{SiO}_2$ : 0.83  $\text{P}_2\text{O}_5$ : 1  $\text{Al}_2\text{O}_3$ : 60  $\text{H}_2\text{O}$ . In a typical synthesis: (1) o-phosphoric acid and d.i. water were first mixed and stirred for 5 min at room temperature. (2) Aluminum hydroxide powder was then slowly added in 5 min under stirring; the slurry was then stirred for 20 min. (3) Fumed silica was added within 10 min and the slurry was stirred for 30 min. (4) Morpholine was added drop by drop under stirring and the slurry was then stirred for 30 min. (5) The Cu-TEPA solution, measured to contain the desired amount of

Cu, was slowly added to the slurry under stirring. (6) The suspension was transferred to a 150 ml PTFE lined autoclave containing a magnetic stir bar and sealed. The autoclave was placed above a stir/heat plate and inside a sand bath. Under stirring (500 rpm), the slurry was aged at room temperature for 24 h to facilitate silica hydrolysis. Subsequently, the sand bath temperature was raised to 200 °C in order to start SAPO-34 crystallization. The synthesis was maintained for 48 h under continuous stirring, and then the sand bath was cooled down to room temperature. (7) The solid product was separated with centrifugation, washed twice with d.i. water, and then dried at 120 °C in flowing  $\text{N}_2$  before calcination in static air at 600 °C for 5 h.

The as-prepared catalysts are designated as Cu1-F and Cu2-F, where “F” stands for fresh samples. Cu loadings and Al/P/Si contents of the fresh samples were measured with Inductively Coupled Plasma Atomic Emission Spectroscopy (ICP-AES) conducted at Galbraith Laboratories (Knoxville, TN, USA), with the results displayed in Supplementary Table 1. Low-temperature hydrothermal aging of the fresh catalysts was performed in flowing air containing 10% of water vapor at 70 °C for 48 h. The samples thus generated are named Cu1-LT and Cu2-LT, where “LT” stands for low-temperature aging. High-temperature hydrothermal aging was performed in flowing air containing 10% of water vapor at 800 °C for 16 h. These samples are named Cu1-HT and Cu2-HT, where “HT” stands for high-temperature aging. The fresh samples were also stored in glass vials under typical laboratory environments (~20 °C, relative humidity ~50%) for 240 days. These samples are named Cu1-S and Cu2-S, where “S” stands for stored samples.

**X-Ray diffraction (XRD) measurements.** Ex situ powder X-Ray diffraction (XRD) was performed on a PANalytical X’Pert MPD system with a vertical  $\Theta$ - $\Theta$  goniometer (190-mm radius). The X-ray source is a long-fine-focus, ceramic X-ray tube with a Cu anode, operating at 40 kV and 50 mA. The data were collected with  $2\theta$  ranging from 5 to 50° using a step size of 0.02°. In situ XRD was performed on a PANalytical X’Pert MPD system with a vertical  $\Theta$ - $\Theta$  goniometer (220 mm radius). The X-ray source was a long-fine-focus, ceramic X-ray tube with a Cu anode, operating at 45 kV and 40 mA. The sample was placed on a sample stage (Anton Paar HTK 1200, temperature range 20–1000 °C) and heated stepwise in dry  $\text{N}_2$  flow from 20 °C to higher temperatures at 20 °C intervals. At each temperature, scanning was conducted from 10 to 50° with a step size of 0.02°.

**Surface area and pore volume measurements.** Surface areas (BET method) and micropore volumes (t-plot method) of the samples were measured with a Quantachrome Autosorb-6 analyzer. Prior to measurements, the samples were dehydrated under a vacuum overnight at 250 °C. Note that Cu1-S loses its crystallinity after this treatment.

**Temperature-programmed reduction with  $\text{H}_2$ .** Temperature-programmed reduction with  $\text{H}_2$  ( $\text{H}_2$ -TPR) was performed on a Micromeritics AutoChem II analyzer. After purging the hydrated samples (samples stored in air and saturated with moisture) with pure  $\text{N}_2$  at 10 mL/min at room temperature for 30 min, TPR was carried out in 5%  $\text{H}_2/\text{Ar}$  at a flow rate of 30 mL/min. Temperature was ramped



linearly from ambient to 650 °C at 10 K/min, and H<sub>2</sub> consumption was monitored with a TCD detector. H<sub>2</sub> consumption was quantified using Ag<sub>2</sub>O and CuO standards.

**NH<sub>3</sub> temperature-programmed desorption.** NH<sub>3</sub> temperature-programmed desorption (NH<sub>3</sub>-TPD) was used to measure NH<sub>3</sub> adsorption on Lewis and Brønsted acid sites in the catalysts. NH<sub>3</sub>-TPD was carried out using our SCR reaction system, with NH<sub>3</sub> detection via an online MKS 2030 FTIR analyzer. A total of 60 mg of catalyst (60–80 mesh) was used for each measurement, and the following experimental steps were followed: (1) heat the sample to 550 °C in O<sub>2</sub>/N<sub>2</sub> (300 sccm, 14% O<sub>2</sub>) and keep at 550 °C for 30 min; (2) stop O<sub>2</sub> flow, maintain N<sub>2</sub> flow, and cool sample to NH<sub>3</sub> adsorption temperatures of 100 °C; (3) adsorb NH<sub>3</sub> (500 ppm in N<sub>2</sub>) until outlet NH<sub>3</sub> concentrations remain constant for 1 h; (4) turn off the NH<sub>3</sub> flow and purge with N<sub>2</sub> for 1 h at the adsorption temperature; and (5) while measuring NH<sub>3</sub> concentrations in the outlet, ramp from the adsorption temperature to 600 °C at 10 °C/min, and maintain at 600 °C until NH<sub>3</sub> desorption becomes undetectable.

**Electron paramagnetic resonance (EPR) measurements.** Electron paramagnetic resonance (EPR) experiments were carried out on a Bruker E580 X-band spectrometer. Powder samples (~15 mg) were contained in 4 mm OD quartz tubes. For CW experiments it is equipped with a SHQE resonator and a continuous flow cryostat. During spectral acquisition, microwave power was 200 mW, and the frequency was 9.86 GHz. The field was swept 1500 G in 84 s and modulated at 100 kHz with a 5 G amplitude. A time constant of 20 ms was used. The isolated Cu(II) contents were quantified using the following method. Typically, spectra acquired at 125 K were first double-integrated to obtain signal areas, which are proportional to EPR active isolated Cu(II) contents. To quantify these, a series of standard solutions with different isolated Cu(II) concentrations were prepared by dissolving Cu(NO<sub>3</sub>)<sub>2</sub>·2.5H<sub>2</sub>O and imidazole (Sigma-Aldrich, 99%) in ethylene glycol (Sigma-Aldrich, 99.8%). Imidazole was used here to coordinate with Cu(II) ions to prevent formation of EPR silent Cu dimers. The linear calibration curve generated using the integral areas and Cu contents of the standard solutions was then used for quantification of isolated Cu(II) in the catalysts. For pulsed EPR experiments the spectrometer was outfitted with an MD-5 dielectric resonator and an Oxford liquid helium continuous flow cryostat which maintained the temperature at 10 K. Typical parameters for HYSCORE experiments with a pi/2-tau-pi/2-t1-pi-t2-pi/2 sequence were: pi/2 = 8 ns, pi = 16 ns, tau = 128 ns and t1, t2 ranging from 200 ns to 2248 ns in 128 steps of 16 ns. The recycle delay was ~500 us and typically 1024 shots were collected for each delay.

**Nuclear magnetic resonance (NMR) measurements.** Nuclear magnetic resonance (NMR) experiments were performed on powder samples either fully hydrated or after evacuation at 10<sup>-3</sup> Torr and 150 °C for 12 h (dehydrated). Note again that this dehydration treatment causes Cu1-S to lose its crystallinity. All experiments were conducted under a dry N<sub>2</sub> atmosphere. <sup>27</sup>Al and <sup>31</sup>P direct polarization (DP) experiments were carried out on a Varian VNMRs system operating at 14.1 T utilizing a 4 mm TR probe operating in DR mode. Direct polarization experiments with <sup>1</sup>H decoupling were conducted utilizing a <sup>1</sup>H frequency of 599.8517, continuous wave decoupling fields of 45 kHz for both <sup>27</sup>Al and <sup>31</sup>P, and <sup>27</sup>Al and <sup>31</sup>P frequencies of 156.3056 and 242.8129, respectively. Calibrated pi/20 pulses of 0.50 us, spinning frequency of 15 kHz, a 50 kHz spectral window, 2048 complex points, and a 2 s pulse delay were utilized to acquire 512 time-averaged scans for <sup>27</sup>Al DP experiments. Time domain free induction decays were apodized with exponential functions corresponding to 200 Hz of Lorentzian line broadening prior to Fourier transformation. A pi/2 pulse of 5.0 us, a spinning frequency of 15 kHz, 100 kHz spectral window, 4096 complex points, and a 240 s pulse delay were utilized to acquire 4 time-averaged scans for <sup>31</sup>P DP experiments. Time domain free induction decays were apodized with exponential functions corresponding to 100 Hz of Lorentzian line broadening prior to Fourier transformation. <sup>29</sup>Si DP experiments were carried out on a Varian VNMRs system operating at 20T utilizing a 4 mm TR probe operating in DR mode. Direct polarization experiments with <sup>1</sup>H decoupling were conducted utilizing a <sup>1</sup>H frequency of 849.7299 and a continuous wave decoupling field of 50 kHz. A total of 640 time-averaged transients were acquired utilizing a pi/2 pulse of 6.0 us at a <sup>29</sup>Si frequency of 168.8018, spinning frequency of 10 kHz, a 50 kHz spectral window, 5024 complex points, and a 120 s pulse delay. Time domain free induction decays were apodized with exponential functions corresponding to 300 Hz of Lorentzian line broadening.

**SCR reaction tests.** NH<sub>3</sub>-SCR reaction was measured using a plug flow reaction system described elsewhere<sup>17</sup>. Powder samples were pressed, crushed and sieved (60–80 mesh) prior to use. For standard SCR, the feed gas contained 360 ppm NO, 360 ppm NH<sub>3</sub>, 14% O<sub>2</sub>, 2.5% H<sub>2</sub>O and balance N<sub>2</sub>. H<sub>2</sub>O was introduced to the feed by passing balance gas N<sub>2</sub> through a water saturator. All of the gas lines were maintained at ~120 °C to avoid water condensation. The total gas flow was 1000 sccm. For “light-off” experiments, 200 mg catalyst was used, and the gas hourly space velocity (GHSV) was estimated to be ~200,000 h<sup>-1</sup>. For low-temperature

kinetic studies, NO<sub>x</sub> and NH<sub>3</sub> conversions were maintained low (<15%). In this case, 60 mg catalyst was used, resulting in a GHSV of ~650,000 h<sup>-1</sup>. Concentrations of reactants and products were measured by an online MKS 2030 FTIR analyzer. Prior to reaction testing, the catalysts were first pretreated in a 14% O<sub>2</sub>/N<sub>2</sub> flow for 1 h at 500 °C. The following equations were used to calculate NO<sub>x</sub> and NH<sub>3</sub> conversions:

$$\text{NO}_x \text{ conversion\%} = \frac{(\text{NO} + \text{NO}_2)_{\text{inlet}} - (\text{NO} + \text{NO}_2 + \text{N}_2\text{O})_{\text{outlet}}}{(\text{NO} + \text{NO}_2)_{\text{inlet}}} \times 100, \quad (1)$$

$$\text{NH}_3 \text{ conversion\%} = \frac{(\text{NH}_3)_{\text{inlet}} - (\text{NH}_3)_{\text{outlet}}}{(\text{NH}_3)_{\text{inlet}}} \times 100. \quad (2)$$

**Theoretical calculations with DFT.** All periodic DFT calculations were carried out employing a mixed Gaussian and plane wave basis sets implemented in the CP2K code<sup>32</sup>. Core electrons were represented with norm-conserving Goedecker-Teter-Hutter pseudopotentials<sup>33–35</sup>, and the valence electron wavefunction was expanded in a triple-zeta basis set with polarization functions<sup>36</sup> along with an auxiliary plane wave basis set with an energy cutoff of 400 Ry. The generalized gradient approximation exchange-correlation functional of Perdew, Burke, and Ernzerhof (PBE)<sup>37</sup> was used. The adsorption and reaction intermediate configurations were optimized with the Broyden-Fletcher-Goldfarb-Shanno (BGFS) algorithm with SCF convergence criteria of 1.0 × 10<sup>-8</sup> au. The calculated total energy difference was negligible (<0.01 eV) when the maximum force convergence criteria of 0.001 hartree/bohr was used. The short-range van der Waals dispersion interaction was compensated using semi-empirical DFT-D3 scheme<sup>38</sup>.

The SAPO-34 zeolite structure was modeled using two hexagonal unit cell with the size parameters of 13.6433 × 23.6310 × 14.8205 Å<sup>3</sup>. To mimic experimental Cu1 composition (Cu<sub>0.34</sub>Al<sub>17.4</sub>P<sub>11.7</sub>Si<sub>6.9</sub>O<sub>72</sub>), the simulated system shown in Supplementary Fig. 18 was constructed with a composition of CuAl<sub>36</sub>P<sub>24</sub>Si<sub>12</sub>H<sub>12</sub>O<sub>145</sub> where the Si/Al/P ratio was 1:3:2 and one proton (H<sup>+</sup>) at a Brønsted acidic site (BAS) was replaced by a [Cu<sup>II</sup>(OH)]<sup>+</sup>, which was located in the window of eight membered ring (8MR) of SAPO-34 zeolite<sup>23,39–41</sup>. It has been well-established that confinement and steric hindrance can strongly affect the stabilities of adsorption states and reaction intermediates in the zeolites<sup>42–46</sup>. As such, Gibbs free energy changes (ΔG) that account for the important entropic contribution (ΔS) and zero-point energy (ZPE) corrections were calculated using statistical thermodynamic method, with details provided elsewhere<sup>47</sup>. Transition states of elementary reaction steps were located using the climbing image nudged elastic band (CI-NEB) method<sup>48,49</sup> with seven intermediate images along the reaction pathway between initial and final states. The identified transition states were confirmed by a vibrational analysis.

## Data availability

All data supporting this study and its findings are available within the article and its Supplementary Information or from the corresponding author upon reasonable request.

Received: 9 November 2018 Accepted: 29 January 2019

Published online: 08 March 2019

## References

- Nova, I. & Tronconi, E. *Urea-SCR Technology for deNO<sub>x</sub> After Treatment of Diesel Exhausts*. (Springer Science + Business Media, New York, USA, 2014).
- Gao, F., Kwak, J. H., Szanyi, J. & Peden, C. H. F. Current understanding of Cu-exchanged chabazite molecular sieves for use as commercial diesel engine DeNO(x) catalysts. *Top Catal.* **56**, 1441–1459 (2013).
- Beale, A. M., Gao, F., Lezcano-Gonzalez, I., Peden, C. H. F. & Szanyi, J. Recent advances in automotive catalysis for NO<sub>x</sub> emission control by small-pore microporous materials. *Chem. Soc. Rev.* **44**, 7371–7405 (2015).
- Wang, D. et al. A comparison of hydrothermal aging effects on NH<sub>3</sub>-SCR of NO<sub>x</sub> over Cu-SSZ-13 and Cu-SAPO-34 catalysts. *Appl. Catal. B-Environ.* **165**, 438–445 (2015).
- Leistner, K. et al. Comparison of Cu/BEA, Cu/SSZ-13 and Cu/SAPO-34 for ammonia-SCR reactions. *Catal. Today* **258**, 49–55 (2015).
- Woo, J. et al. Effect of various structure directing agents (SDAs) on low-temperature deactivation of Cu/SAPO-34 during NH<sub>3</sub>-SCR reaction. *Catal. Sci. Technol.* **8**, 3090–3106 (2018).
- Leistner, K. & Olsson, L. Deactivation of Cu/SAPO-34 during low-temperature NH<sub>3</sub>-SCR. *Appl. Catal. B-Environ.* **165**, 192–199 (2015).
- Wang, J. et al. Improvement of low-temperature hydrothermal stability of Cu/SAPO-34 catalysts by Cu<sup>2+</sup> species. *J. Catal.* **322**, 84–90 (2015).
- Briend, M., Vomscheid, R., Peltre, M. J., Man, P. P. & Barthomeuf, D. Influence of the choice of the template on the short-term and long-term stability of SAPO-34 zeolite. *J. Phys. Chem.* **99**, 8270–8276 (1995).



10. Vomscheid, R., Briend, M., Peltre, M. J., Man, P. P. & Barthomeuf, D. The role of the template in directing the Si distribution in SAPO zeolites. *J. Phys. Chem.* **98**, 9614–9618 (1994).
11. Vennessstrom, P. N. R. et al. Migration of Cu Ions in SAPO-34 and its impact on selective catalytic reduction of NO<sub>x</sub> with NH<sub>3</sub>. *ACS Catal.* **3**, 2158–2161 (2013).
12. Gao, F., Walter, E. D., Washton, N. M., Szanyi, J. & Peden, C. H. F. Synthesis and evaluation of Cu-SAPO-34 catalysts for ammonia selective catalytic reduction. 1. Aqueous solution ion exchange. *ACS Catal.* **3**, 2083–2093 (2013).
13. Gao, F., Walter, E. D., Washton, N. M., Szanyi, J. & Peden, C. H. F. Synthesis and evaluation of Cu-SAPO-34 catalysts for NH<sub>3</sub>-SCR 2: solid-state ion exchange and one-pot synthesis. *Appl. Catal. B-Environ.* **162**, 501–514 (2015).
14. Ren, L. M. et al. Designed copper-amine complex as an efficient template for one-pot synthesis of Cu-SSZ-13 zeolite with excellent activity for selective catalytic reduction of NO<sub>x</sub> by NH<sub>3</sub>. *Chem. Commun.* **47**, 9789–9791 (2011).
15. Martinez-Franco, R., Moliner, M., Concepcion, P., Thogersen, J. R. & Corma, A. Synthesis, characterization and reactivity of high hydrothermally stable Cu-SAPO-34 materials prepared by “one-pot” processes. *J. Catal.* **314**, 73–82 (2014).
16. Schweiger, A. Pulsed electron-spin-resonance spectroscopy - basic principles, techniques, and examples of applications. *Angew. Chem. Int. Ed.* **30**, 265–292 (1991).
17. Gao, F. et al. Understanding ammonia selective catalytic reduction kinetics over Cu/SSZ-13 from motion of the Cu ions. *J. Catal.* **319**, 1–14 (2014).
18. Song, J. et al. Toward rational design of Cu/SSZ-13 selective catalytic reduction catalysts: implications from atomic-level understanding of hydrothermal stability. *ACS Catal.* **7**, 8214–8227 (2017).
19. Carl, P. J. & Larsen, S. C. EPR study of copper-exchanged zeolites: effects of correlated g- and A-strain, Si/Al ratio, and parent zeolite. *J. Phys. Chem. B* **104**, 6568–6575 (2000).
20. Schweiger, A. & Jeschke, G. *Principles of Pulse Electron Paramagnetic Resonance*. 1st edition (Oxford University Press, New York, USA, 2001).
21. Carl, P. J., Vaughan, D. E. W. & Goldfarb, D. Interactions of Cu(II) ions with framework Al in high Si: Al zeolite Y as determined from X- and W-band pulsed EPR/ENDOR spectroscopies. *J. Phys. Chem. B* **106**, 5428–5437 (2002).
22. Luo, J. Y. et al. New insights into Cu/SSZ-13 SCR catalyst acidity. Part I: Nature of acidic sites probed by NH<sub>3</sub> titration. *J. Catal.* **348**, 291–299 (2017).
23. Paolucci, C. et al. Catalysis in a cage: condition-dependent speciation and dynamics of exchanged Cu cations in SSZ-13 zeolites. *J. Am. Chem. Soc.* **138**, 6028–6048 (2016).
24. Vennessstrom, P. N. R. et al. Influence of lattice stability on hydrothermal deactivation of Cu-ZSM-5 and Cu-IM-5 zeolites for selective catalytic reduction of NO<sub>x</sub> by NH<sub>3</sub>. *J. Catal.* **309**, 477–490 (2014).
25. Fjermestad, T., Svelle, S. & Swang, O. Mechanistic comparison of the dealumination in SSZ-13 and the desilication in SAPO-34. *J. Phys. Chem. C* **117**, 13442–13451 (2013).
26. Li, H., Paolucci, C. & Schneider, W. F. Zeolite adsorption free energies from ab initio potentials of mean force. *J. Chem. Theory Comput.* **14**, 929–938 (2018).
27. Tan, J. et al. Crystallization and Si incorporation mechanisms of SAPO-34. *Micro. Mesopor. Mat.* **53**, 97–108 (2002).
28. Buchholz, A., Wang, W., Arnold, A., Xu, M. & Hunger, M. Successive steps of hydration and dehydration of silicoaluminophosphates H-SAPO-34 and H-SAPO-37 investigated by in situ CF MAS NMR spectroscopy. *Micro. Mesopor. Mat.* **57**, 157–168 (2003).
29. Briend, M., Vomscheid, R., Peltre, M. J., Man, P. P. & Barthomeuf, D. Influence of the choice of the template on the short-term and long-term stability of SAPO-34 zeolite. *J. Phys. Chem.* **99**, 8270–8276 (1995).
30. Prakash, A. M. & Unnikrishnan, S. Synthesis of SAPO-34 - high-silicon incorporation in the presence of morpholine as template. *J. Chem. Soc. Faraday Trans.* **90**, 2291–2296 (1994).
31. Martinez-Franco, R., Moliner, M., Franch, C., Kustov, A. & Corma, A. Rational direct synthesis methodology of very active and hydrothermally stable Cu-SAPO-34 molecular sieves for the SCR of NO<sub>x</sub>. *Appl. Catal. B-Environ.* **127**, 273–280 (2012).
32. VandeVondele, J. et al. Quickstep: fast and accurate density functional calculations using a mixed Gaussian and plane waves approach. *Comput. Phys. Commun.* **167**, 103–128 (2005).
33. Goedecker, S., Teter, M. & Hutter, J. Separable dual-space Gaussian pseudopotentials. *Phys. Rev. B* **54**, 1703–1710 (1996).
34. Hartwigsen, C., Goedecker, S. & Hutter, J. Relativistic separable dual-space Gaussian pseudopotentials from H to Rn. *Phys. Rev. B* **58**, 3641–3662 (1998).
35. Krack, M. & Parrinello, M. All-electron ab-initio molecular dynamics. *Phys. Chem. Chem. Phys.* **2**, 2105–2112 (2000).
36. VandeVondele, J. & Hutter, J. Gaussian basis sets for accurate calculations on molecular systems in gas and condensed phases. *J. Chem. Phys.* **127**, 114105 (2007).
37. Perdew, J. P., Burke, K. & Ernzerhof, M. Generalized gradient approximation made simple. *Phys. Rev. Lett.* **77**, 3865 (1996).
38. Grimme, S., Antony, J., Ehrlich, S. & Krieg, H. A consistent and accurate ab initio parametrization of density functional dispersion correction (DFT-D) for the 94 elements H-Pu. *J. Chem. Phys.* **132**, 154104 (2010).
39. Paolucci, C. et al. Isolation of the copper redox steps in the standard selective catalytic reduction on Cu-SSZ-13. *Angew. Chem. Int. Ed.* **53**, 11828–11833 (2014).
40. Janssens, T. V. W. et al. A consistent reaction scheme for the selective catalytic reduction of nitrogen oxides with ammonia. *ACS Catal.* **5**, 2832–2845 (2015).
41. Zhang, R. Q. et al. NO chemisorption on Cu/SSZ-13: a comparative study from infrared spectroscopy and DFT calculations. *ACS Catal.* **4**, 4093–4105 (2014).
42. Bhan, A., Gounder, R., Macht, J. & Iglesia, E. Entropy considerations in monomolecular cracking of alkanes on acidic zeolites. *J. Catal.* **253**, 221–224 (2008).
43. Gounder, R. & Iglesia, E. Catalytic consequences of spatial constraints and acid site location for monomolecular alkane activation on zeolites. *J. Am. Chem. Soc.* **131**, 1958–1971 (2009).
44. Gounder, R. & Iglesia, E. The roles of entropy and enthalpy in stabilizing ion-pairs at transition states in zeolite acid catalysis. *Acc. Chem. Res.* **45**, 229–238 (2012).
45. Jones, A. J. & Iglesia, E. Kinetic, spectroscopic, and theoretical assessment of associative and dissociative methanol dehydration routes in zeolites. *Angew. Chem. Int. Ed.* **53**, 12177–12181 (2014).
46. Jones, A. J., Zones, S. I. & Iglesia, E. Implications of transition state confinement within small voids for acid catalysis. *J. Phys. Chem. C* **118**, 17787–17800 (2014).
47. Psogiannakis, G., St-Amant, A. & Ternan, M. Methane oxidation mechanism on Pt(111): a cluster model DFT study. *J. Phys. Chem. B* **110**, 24593–24605 (2006).
48. Henkelman, G., Uberuaga, B. P. & Jonsson, H. A climbing image nudged elastic band method for finding saddle points and minimum energy paths. *J. Chem. Phys.* **113**, 9901–9904 (2000).
49. Mills, G., Jonsson, H. & Schenter, G. K. Reversible work transition-state theory - application to dissociative adsorption of hydrogen. *Surf. Sci.* **324**, 305–337 (1995).

## Acknowledgements

The authors gratefully acknowledge the US Department of Energy (DOE), Energy Efficiency and Renewable Energy, Vehicle Technologies Office for the support of this work. Computing time was granted by a user proposal at the William R. Wiley Environmental Molecular Sciences Laboratory (EMSL) and by the National Energy Research Scientific Computing Center (NERSC). The experimental studies described in this paper were performed in the EMSL, a national scientific user facility sponsored by the DOE's Office of Biological and Environmental Research and located at Pacific Northwest National Laboratory (PNNL). PNNL is operated for the US DOE by Battelle.

## Author contributions

F.G. conceptualized the research effort. A.W. and Y.L.W. synthesized the Cu-SAPO-34 catalysts. A.W. conducted all of the SCR reaction measurements. A.W. and F.G. analyzed the reaction data. A.W. and E.D.W. performed 1D and 2D EPR measurements and spectra analysis. Y.C. performed 2D EPR spectra simulations. N.M.W. performed NMR measurements and data analysis. T.V. conducted in situ XRD measurements and data analysis. D.M. performed DFT simulations. All authors contributed towards data interpretation. F.G., E.D.W., and D.M. drafted the initial manuscript. All authors reviewed and edited the manuscript and supplementary materials. Particularly, C.H.F.P., Y.W., and J.S. made extensive modifications of the initial manuscript. F.G. and C.H.F.P. finalized the manuscript.

## Additional information

**Supplementary Information** accompanies this paper at <https://doi.org/10.1038/s41467-019-09021-3>.

**Competing interests:** The authors declare no competing interests.

**Reprints and permission** information is available online at <http://npg.nature.com/reprintsandpermissions/>

**Journal peer review information:** *Nature Communications* thanks the anonymous reviewers for their contribution to the peer review of this work. Peer reviewer reports are available.

**Publisher's note:** Springer Nature remains neutral with regard to jurisdictional claims in published maps and institutional affiliations.



**Open Access** This article is licensed under a Creative Commons Attribution 4.0 International License, which permits use, sharing, adaptation, distribution and reproduction in any medium or format, as long as you give appropriate credit to the original author(s) and the source, provide a link to the Creative Commons license, and indicate if changes were made. The images or other third party material in this article are included in the article's Creative Commons license, unless indicated otherwise in a credit line to the material. If material is not included in the article's Creative Commons license and your intended use is not permitted by statutory regulation or exceeds the permitted use, you will need to obtain permission directly from the copyright holder. To view a copy of this license, visit <http://creativecommons.org/licenses/by/4.0/>.

© The Author(s) 2019